Supporting Information for "Basal Melting Variability of the Ross Ice Shelf from Mixing Ratios of Simulated Water Masses (1993-2018) and Potential Climatic Drivers"

Enrico Pochini[12] *

Andrea Bergamasco[3]

Florence Colleoni[1]

Manuel Bensi[1]

Giorgio Budillon[4]

Pasquale Castagno[5]

Michael S. Dinniman[6]

Pierpaolo Falco[7]

Emanuele Forte[2]

Vedrana Kovačević[1]

Stefanie L. Mack[8]

[1]National Institute of Oceanography and Applied Geophysics (OGS), Borgo Grotta Gigante, 42/c, 34010 Sgonico (TS), Italy

[2]University of Trieste, (UniTS), Piazzale Europa, 1, 34127 Trieste (TS), Italy

[3]National Research Council - Institute of Polar Sciences, (CNR-ISP), c/o Scientific Campus - Ca' Foscari University Venice - Via Torino, 155 - 30172 Venezia Mestre (VE), Italy

[4]University of Naples Parthenope, (UniParthenope), Via Ammiraglio Ferdinando Acton, 38, 80133 Naples (NA), Italy

January 3, 2026, 12:53pm

[5]University of Messina, Piazza Pugliatti, 1, 98122 Messina ME, Italy

[6]Center for Coastal Physical Oceanography, Old Dominion University (CCPO-ODU), 4111 Monarch Way, Norfolk, VA 23508-2559, USA

[7]Marche Polytechnic University, (UNIVPM), Via Lodovico Menicucci, 6, 60121 Ancona (AN), Italy

[8]University of Tokyo, 7-3-1, Hongo, Bunkyo-ku, Tokyo 113-8654 Japan

Contents of this file

1. Text S1 to S8
2. Figures S1 to S14
3. Tables S1 to S3

Introduction

This document contains technical aspects related to the model and experimental setup, a more detailed description of the implementation of the mixing method, a comparison of model outputs with observations, a description of the sea ice budget calculation and comparison with observations, a comparison with Ross Sea simulations carried out with ROMS (Dinniman et al., 2018). It also contains supplementary figures and tables referred to in the text.

---

[*]Now at University of Alberta, dept.
Earth and Atmospheric Sciences,
Edmonton, Alberta, Canada

Text S1. Impact of teleconnections on the Ross Sea

Several remote drivers play a role in the Ross Sea interannual and decadal variability, either directly or indirectly. The Amundsen Sea Low (ASL), the Southern Annular Mode (SAM), and the tropical teleconnections related to El-Niño Southern Oscillation (ENSO) are known to influence the climate on the coasts of Antarctica (Li et al., 2021), the ice shelves (Paolo et al., 2018), and sea ice (Meehl et al., 2016). The ASL in its positive phase (high pressure, weakened ASL) induces an anticyclonic anomaly, which weakens the coastal easterlies in the Amundsen Sea region (Holland & Kwok, 2012). This would produce a decreased sea ice transport into the Ross Sea (Figure S1a). The ASL also induces a southerly winds anomaly over the Ross Sea, which enhances, in its negative phase (low pressure, strengthened ASL), the export of sea ice from the Ross Sea to the open ocean (Li et al., 2021). Interestingly, the impact of the ASL on the Ross Sea sea ice concentration appears to be stronger during the sea ice retreat phase, (Raphael et al., 2019), therefore the northerly wind anomalies seem to be more important in driving ice retreat than the southerly anomalies in driving the advance. The ASL has 5 indices, which indicate: the minimum mean-sea level pressure, which defines the ASL, the sector-averaged pressure, the relative pressure difference between the two, and finally the latitude and longitude displacement of the pressure minimum. The Southern Annular Mode (SAM) measures the strength of the westerlies in the open ocean; in its positive phase, it causes a southward shift of the westerlies, which weakens the coastal easterlies (Spence et al., 2014). El Niño Southern Oscillation (ENSO) has an impact on regional atmospheric circulation and heat delivery to the Pacific coasts of Antarctica (J. Liu et al., 2002; Paolo et al., 2018), and it is known to perturb the ASL pressure field by a

train of stationary Rossby waves (Turner, 2004). A positive phase ENSO, would produce a positive pressure anomaly over the ASL region, associated with an anticyclonic wind anomaly, thereby weakening the ASL. ENSO is generally defined from the tropical surface temperature by the Ocean Niño Index (ONI), or the Niño 3.4 index, or from mean-sea level pressure gradient across the Pacific, by the Southern Oscillation Index (SOI); notice that the SOI is negative for positive ENSO phases, contrary to the ONI and Niño 3.4. Other indices, which are defined separately from ENSO, account for longer timescale surface temperature variability in the Pacific Ocean, such as the Pacific Decadal Oscillation (PDO) and Interdecadal Pacific Oscillation (IPO) (Yuan, 2004; Meehl et al., 2016; Li et al., 2021). The impact of the ASL, SAM, and ENSO is shown on the regressed pressure field (Figure S1a-f): the geostrophic near-surface atmospheric circulation associated with a positive pressure anomaly is anticyclonic (i.e., counterclockwise in the Southern Hemisphere) and vice versa for a negative anomaly. A positive pressure anomaly on the Amundsen Sea weakens the ASL. Wind anomalies also impact sea ice transport (Figure S1g-l); in fact, the ASL and ENSO in their positive phases produce a bipolar anomalous distribution centered in the Bellingshausen Sea (Yuan, 2004; Li et al., 2021), although the impact of the ASL is complicated by the location of the ASL minimum during the advance and retreate phases of sea ice (Raphael et al., 2019).

Text S2. MITgcm Ross Sea implementation

The model physics and parameterizations are described in detail in the first author's PhD dissertation (Pochini, 2022, Chapter 2). Here, the most important aspects of the simulations are reported. In the present study, we implement a regional configuration of the Massachusetts Institute of Technology general circulation model (MITgcm, Marshall,

Adcroft, et al., 1997; Marshall, Hill, et al., 1997) on the Ross Sea sector, Antarctica (Figure 1a). The model domain includes the Ross Ice Shelf (RIS) cavity, smaller glaciers found in the Ross Sea, and a part of the Amundsen Sea region. The model grid, bathymetry (Figure 1a), and ice shelf drafts are generated by interpolating the Bedmap2 dataset (Fretwell et al., 2013) on a cartesian grid at 5-km horizontal resolution obtained with an oblique stereographic projection with the OBLIMAP-2 mapping tool (Reerink et al., 2016). The grid has 50 vertical levels of variable thickness, arranged in z-coordinate levels. To increase the vertical resolution over the Ross Sea continental shelf and inside the RIS cavity, the upper 32 layers are refined, with thickness varying from 10 m at the surface and 50 m near the continental sea floor, and vertical resolution decreases at greater depth. The model resolution is deemed to be eddy-permitting at 5-km resolution and was run in hydrostatic mode.

The MITgcm is able to resolve the sharp change in water column thickness across the ice shelf front without additional smoothing. It also allows partially-filled cells to improve the vertical resolution of the ice shelves draft and seafloor bathymetry (Adcroft et al., 1997; Losch, 2008). Inside the RIS cavity, the seafloor bathymetry and the ice shelf draft were pre-processed using the python package `https://github.com/knaughten/mitgcm_python` in order to avoid problematic conditions, such as the ice shelf draft intersecting with the bathymetry, and to remove isolated ocean grid points, potentially found in shallow regions near the coast or the grounding line. A commonly used technique called "digging" is applied. It consists of artificially deepening the bathymetry where the water column is too shallow, e.g., close to the ice sheet grounding line, to ensure that each tracer node has a top and a bottom velocity node to allow minimal water vertical circulation.

Basal melting of the ice shelf base is calculated based on the three-formulation equation (Hellmer & Olbers, 1989; Holland & Jenkins, 1999; Jenkins et al., 2001; Losch, 2008). This formulation considers heat and salt exchange, accounting for horizontal oceanic velocities and turbulent coefficients, from an ocean mixed layer, through a boundary layer at the ice-shelf ocean interface. The MITgcm thus accounts for the effect of freshwater fluxes in terms of changes in temperature and a virtual salinity flux that impacts buoyancy, which, however, conserves mass. A quadratic-law drag (drag $\sim u^2$) is applied to the stress in ocean-sea bed and ocean-ice shelf boundaries ($C_d = 1.5 \cdot 10^{-3}$, See Table S3, model parameters). A free-slip condition was set at the ice shelf-ocean boundary for stress calculation (tangential currents not constrained to be $\equiv 0$), whereas a no-slip condition was prescribed for stress formulation at the seabed. A constant geothermal heat flux is provided after Shapiro and Ritzwoller (2004). The sea ice module is interactive and fully coupled to the ocean dynamics and climate (Losch et al., 2010). The dynamic sea-ice solver uses the Line Successive over Relaxation (LSR) method, with seven thickness classes. Model parameters are set and adjusted following a setup for a run in the Weddell Sea and the Filchner-Ronne Ice Shelf (`https://github.com/knaughten/UaMITgcm`).

Text S3. Open boundary and atmospheric conditions: ERA5, GLORYS12V1

Atmospheric forcing from ERA5 is provided on a nominal 31-km horizontal grid. The fields used to force the MITgcm are: surface pressure, wind velocity, temperature, and specific humidity at 2-meters height, surface precipitation flux, downwelling shortwave, and longwave radiation fluxes. All the fields are interpolated onto the Ross Sea grid by means of the OBLIMAP-2 mapping tool (Reerink et al., 2016). A smoothing filter is

applied to reduce the checkerboard effect due to the downscaling from the ERA5 31-km grid to the higher-resolved 5-km grid of the Ross Sea. Near-surface (2 m) specific humidity is obtained by calculating the saturation specific humidity at the dewpoint temperature. Calculations use near-surface temperature and the surface pressure, following the method indicated in the operational manual of the Integrated Forecasting System of the European Centre for Medium-Range Weather Forecasts (Part IV: "Physical Processes", Chapter 7, section 7.2.1b, Eq.s 7.4 and 7.5):

$$q_{sat} = \frac{\frac{R_{dry}}{R_{vap}} e_{sat}(T)}{p - (1 - \frac{R_{dry}}{R_{vap}}) e_{sat}(T)} \quad (1)$$

$$e_{sat} = a_1 \exp\left\{a_3 \frac{T - T_0}{T - a_4}\right\} \quad (2)$$

The saturation quantities are those obtained when T is substituted by the dewpoint temperature T_{dew}. The constants are: (a_1 = 611.21 Pa, a_3 = 17.502 and a_4 = 32.19 K) for saturation over water.

10-meter wind zonal and meridional components were rotated to be aligned with the cartesian grid axes.

To initialize the ocean state and to provide lateral open boundary conditions where the regional domain connects with the open ocean, we chose the reanalysis GLORYS12V1 (Lellouche et al., 2021), an ocean reanalysis product of the Copernicus Marine Environment Monitoring Service (CMEMS), available at `https://marine.copernicus.eu/access-data`. At the open boundaries, a sponge layer of 40 km (8 grid cells) thickness

is applied to 3D ocean values, whereas no sponge layer is applied to sea ice conditions. Lateral open boundaries are treated with a double relaxation-timescale scheme at the inner and outer sides of the sponge of one year and one week, respectively (only one week for sea ice). GLORYS12V1 performance for the representation of several diagnostics, such as upper ocean heat and salt content (0-1500 m), seasonal cycle of salinity, temperature, sea ice extension, and mixed layer depth transport in the Antarctic Circumpolar Current, is among the highest (Uotila et al., 2019; Lellouche et al., 2021). GLORYS12V1 well reproduces the low-frequency variability (interannual and long-term variability) of the sea ice extent both in the Arctic and Antarctic Oceans, thanks to sea-ice data assimilation. A bias is present in both temperature ($\sim +0.75$ °C) and salinity ($\sim +0.2$ psu) in the upper 2000 m between 1993 and 2002 (Lellouche et al., 2018, 2021), which were undocumented at the time the simulations were run. These biases decrease after the start of the ARGO initiative in 2002 to 0.45°C and 0.1 psu in the same layer. The reanalysis is provided on a high-resolution horizontal grid of 1/12° x 1/12° with 75 vertical levels. We interpolate monthly fields of 3D temperature, salinity, horizontal velocities, as well as sea-ice concentration, sea-ice thickness, and sea-ice drift on the MITgcm Ross Sea grid. The vertical levels of the reanalysis are linearly interpolated on the MITgcm vertical levels. Since the reanalysis does not include any data within the Ross Ice Shelf cavity, and because of the paucity of oceanographic data in this region, the ocean fields are extrapolated with a nearest-neighbors algorithm to initialize the sub-ice shelf cavity and the entire domain up to the coastlines and grounding lines.

Text S4. Generalised mixing ratios decomposition

$$\begin{cases} m_1\theta_1 + m_2\theta_2 + m_3\theta_3 + m_4\theta_4 = \theta \\ m_1S_1 + m_2S_2 + m_3S_3 + m_4S_4 = S \\ m_1 + m_2 + m_3 + m_4 = 1 \end{cases} \tag{3}$$

In our case, θ, S in Equation system 3 are the potential temperature and salinity simulated at each grid cell of the water layer in contact with the ice shelf base, schematically represented by the blue dot in Figure 2. The system of equations cannot be solved analytically like in the three endpoint case, and an approximated solution is found by applying a bounded least square method, specifically a Trust Region Reflective algorithm (implemented in the package `scipy.optimize.lsq_linear`), constrained by $0 < m_i < 1$. The system is in the form Ax = b, subject to a lower and upper boundary $x_1 \leq x \leq x_2$. A is the matrix composed of the θ_i, S_i endpoints matrix, x is the solution array m, constrained between $x_1 = 0$ and $x_2 = 1$, and b is the array with the simulated θ, S. The solution is the array of the monthly mixing ratios m_1 to m_4 at each grid cell of the RIS draft.

Text S5. Observations vs simulation

Drygalski Trough

The continental shelf of the Ross Sea is characterized by sea ice formation in the West, by sea ice and meltwater import in the East, and by exchanges of meltwater within the RIS cavity. In the Drygaslki Trough mooring G was deployed to measure outflowing HSSW (becoming RSBW) and inflowing mCDW from the slope. HSSW is produced in the Western Ross and in a polynya opening in front of the RIS, and is exported to most of the Western Ross Sea, the Western half of the RIS cavity, and in the Glomar Chal-

lenger Trough; however, the maximum presence is in the Drygalski Basin and Trough (Figure S5)). It took measurements of temperature between summer 2004–2014 (Figure S8b), with only a small 6 months gap in 2007; the measurements of salinity covered only three years, 2004-2007 (Figure S8b); velocity coverage was extremely patchy (Figure S8 b,c). The mooring captured intrusions of warm mCDW at the bottom on a background of near-freezing temperature (Figure S8b). Warm temperature fluctuations had high amplitude until 2009 and later became more subdued. The model is not able to capture this strong intradaily variability, which we can assert is because this region is strongly affected by tides (Bergamasco et al., 2004; Gordon et al., 2009; Padman et al., 2009). Our model does not include tides and only simulates the background -1.8 °C temperature with weak yearly variability. Measured salinity shows a distinct seasonal cycle associated with sea ice production in the Drygaslki basin during austral autumn and winter, and reaching mooring G with a lag (Figure S8c). Oscillations of 0.1 psu in salinity are observed. Model salinity partially reproduces this yearly cycle, but it shows a salty bias of ∼0.1 psu (Figure S8a,c). This bias may be inherited by GLORYS12V1, but it was undocumented at the time of model setup preparation (Lellouche et al., 2021). Measured salinity lower than 34.7 indicates probable mixing with mCDW and AASW to form DSW.

Glomar Challenger Trough

The Glomar Challenger Trough is the location where most of the water outflowing from the cavity is found. HSSW entering beneath the RIS from the West and mCDW and LSSW entering from the East are cooled and freshened. Two types of ISW are formed: a saltier form originates from HSSW, while a fresher form originates from mCDW outflowing at

different depths (Jacobs et al., 1985; Bergamasco et al., 2002) into the Glomar Challenger Trough. Mooring H1 was placed at this strategic location and was active from 1995 to 2008. This mooring captured, at the bottom layer, the outflows of HSSW in the Glomar Challenger Trough, which is *supercooled* at about -1.9 °C, (0.1°C colder than in the Drygaslki trough, where it reaches the surface freezing point ∼-1.8°C), therefore could be classified as ISW; this water mass mixes with SW on the continental shelf slope (Figure S9). This deep ISW is seen in the vertical section, GCT in Figure S5 beneath the cavity at distance 600 km along the transect, and a second cold core, not *supercooled*, at the depth of the RIS draft, at ∼450 km along the transect. The yearly warming signal is probably caused by increased mCDW advection in summer and by the generally weaker (more mixed) ISW produced by the model with respect to the observations. The θ, S plot shows the bias in salinity as well as the warmer temperature of the bottom water (Figure S9a). Salinity matched well, except for a faster seasonal cycle in the model (Figure S9d). The mooring measured strong anomalies in salinity and currents in autumn 2000, which is likely the result of a large tabular iceberg, B-15A, which detached from the RIS in summer 2000 and was advected oceanward over the Glomar Challenger Trough (Arrigo et al., 2002). A second trunk, B-15B, was advected to the Western Ross Sea but became stuck between Ross Island and a bank. Such features are difficult to model and are currently not implemented in the MITgcm.

Mooring H3 was placed on the continental slope, where the water column is 1200m deep, at the mouth of the Glomar Challenger Trough, one of the main pathways of exported RSBW, and intrusions of CDW (Bergamasco et al., 2002); it took measurements of temperature and current velocity between summer 2005 and summer 2008. Energetic

outflows of RSBW and inflows of CDW are captured by the mooring in the daily bottom (∼1200m) temperature field, – minima and maxima respectively – and are also simulated by the model daily output at that location (Figure S10a); the two water masses cause a > 1 °C fluctuation in the temperature from the Glomar Challenger Trough across the continental shelf break. Both the model and the mooring measures intense and highly variable currents; in particular, the meridional components are between 20-80 cm/s (Figure S10b,c). Such fluctuations are indicative of strong eddying behavior and connected with the variability of the ASF that, in part, regulates these exchanges. Mooring variability also includes the effect of tides, fostering slope currents at longer periods than tidal variability (Padman et al., 2009); tidal forcing was not included in the model. Inter-monthly variability is visible in the time series, superimposed on stronger daily variability. Transects of averaged potential temperature and salinity (Figures S5) show the cold and salty HSSW and RSBW and the warmer mCDW. They capture the stratification and the mixing process that occur at the shelf break, involving also lower salinity AASW (the first 50-150 metres in the water column). Notice that the "V-shaped" ASF, typical of the "cold" (and also "salty") continental shelves, is visible in the Glomar Challenger Trough (GCT in Figure S5, and weakly visible in the Drygalski Trough, Joides Trough; the effect on the CDW intrusions is to strongly mix them with SW. Notice also in the Whales Deep shelf break that the ASF resembles more the "fresh" and "warm" continental shelf and allows more CDW to arrive on the shelf.

Text S6. Direct Observations of the RIS cavity and basal melting

Ocean models capable of resolving the sub-ice shelf cavities can help fill the knowledge gap

that exists in cavity processes because of logistical and technical difficulties in accessing the cavity environments. Direct observations of the sub-ice shelf cavity are extremely scarce and localized over the RIS (Figure 1a, red triangles); nonetheless, they include either direct estimates of basal melting or estimates derived from direct in-situ oceanographic observations. In the northwestern RIS near Ross Island, at site CH-1,2, Arzeno et al. (2014) and Stewart et al. (2019) observed seasonal intrusions of AASW, by a moored array deployed over two months in November-December 2010, and year-round over 2011-2014 respectively. The mooring was deployed under ∼220 m of ice, where bathymetry is ∼800 m below sea level. In the middle of the RIS, at HWD-2, Stevens et al. (2020) measured the properties of the water column in December 2017, under ∼300 m of ice, and seafloor at ∼750 m depth. Begeman et al. (2018) took measurements from the Southwestern grounding line along the Whillans Ice Stream Grounding Zone (WGZ), in summer 2014-2015, under ∼650 m of ice, and seafloor at 675 m depth. Along Siple Coast, recent boreholes were drilled at the Kamb Ice Stream grounding zone, KIS1 (Lawrence et al., 2023), and KIS2 (Whiteford et al., 2022; Horgan et al., 2025), in 2021-2022, under 500 m of ice, and over a seafloor ∼540 m deep. At KIS1 a crevasse in the ice shelf 40 m deep was also sampled, and at KIS2 a subglacial channel 200 m deep was sampled. These areas experience different oceanographic regimes: the Western part of the RIS cavity is flooded by HSSW, which reaches the sites at WGZ and HWD-2, and seasonally AASW intrusions occur at CH-1,2. CLose to the grounding line in Siple Coast, at WGZ, KIS1 and KIS2, the circulation becomes more stagnant, and strongly affected by the subglacial discharge from the grounding line, especially at the Kamb Ice Stream (sites KIS1, KIS2), which drives high, extremely-localized basal melting.

We compared our model daily θS output at the same sites, for the same season as the period of measurement, and including the neighbouring grid points. All measurements were converted from pressure to metres below sea level, and from different definitions of temperature and salinity to potential temperature (ITS-90) and practical salinity (PSS-78), via the Gibbs Sea Water Python package. The results are reported in Figure S3c-f and Figure S4.

We see a partial match with observation at sites CH-1,2 (Figure S3c,d), particularly at depth 385 m, 560 m, and 757 m, where HSSW, AASW, and mixing with MW is shown, although the HSSW appears $\sim$0.05 PSU saltier than the observations. The model, however, does not simulate as well the strongly supercooled ($\sim$ -2 °C) and fresh (34.2 - 34.4) water masses at 225 m, which is extremely close to the ice shelf base. Arzeno et al. (2014) inferred basal melting at two under-ice shelf CH-1,2 mooring sites in the Ross Island region based on observed heat-flux divergence, which yields an average value of 1.2 $\pm$ 0.5 m/y over the two-month summer measurements, consistent with our average melting over the Ross Island region. Stewart, Christoffersen, Nicholls, Williams, and Dowdeswell (2019) took observations for 4 years, the longest recorded, confirming our simulated AASW regime, matching the timing of the maximum of the intrusion, in February, and the melting rate observed: 3 m/y on a January-March average, against the simulated ones that are between 3-3.5 m/y for the same sampled years. At the same site, observed current regime, i.e., inflows during December-February and outflow during the rest of the year (Stewart et al., 2019), matches with our simulated meridional velocity at about 200m depth, the layer at the draft. Notice, however, that the layer immediately beneath it, at 230 m, shows an

inflow intensification during winter, consistent with resumed polynya activity and HSSW inflowing into the cavity during April-October.

In the western-central RIS, observations were collected at sites J9 (Clough & Hansen, 1979; Zotikov, 1979) and at site HWD-2. The model does a reasonable job at reproducing the stratification of the water column at HWD-2 (Figure S3e,f), although the model does not reproduce the very fresh boundary layer about 30 m thick closer the the ice shelf base. The observations at HWD-2 are thought to represent the average oceanographic conditions in the central RIS cavity (Stevens et al., 2020). The evaluated basal melting at site HWD-2 is low, $\sim 0 - 0.09$m/y (Stevens et al., 2020), and compares with our simulated value at ~ 0.04m/y.

At WGZ (Figure S4e,f), the model simulates fairly well the deeper layer salinity and temperature and the stratification, although the observation follows more closely the Gade line than the simulation. Observations of basal melting by an Autonomous phase-sensitive Radio-Echo Sounding (ApRES) were collected over two weeks in January 2015 (Begeman et al., 2018). They show low basal melting near the grounding line, $\sim 0.05 \dashv 0.07 \pm 0.02$ m/y, consistent with slow circulation and predominance of HSSW mixed with high values of MW, despite the strong tidal mixing. In the model, melting at the site investigated ($\sim$ 84.20°S, 164°W), which lies next to the grounding line, is only ~ 0.018 m/y; however, in the nearest grid-point seaward, it ranges 0.3 - 0.4 m/y, implying strong spatial variability and difficulty in resolving circulation in such a shallow and confined environment. However, localized measurements with phase-sensitive radar in a nearby channel at the Southern grounding line, between Mercer and Whillans Ice Stream, revealed extremely high values of basal melting, 15 - 22 m/y (Marsh et al., 2016), which compare with only ~ 0.25 m/y

of simulated basal melting in the 5x5 km cell grid, colocated with the site. This shows how the ice shelf base morphology and the likely presence of subglacial channels greatly enhance localized currents and melting (Jenkins, 2011).

The model, however, does not do a good job at simulating the water masses and circulation at KIS1 (Figure S4a,b), and KIS2 (Figure S4c,d). The simulated water column, there, is almost uniform and close to the *in-situ* freezing point. The subglacial environment at KIS1 and KIS2 is dominated by deep crevasses and a subglacial drainage system that cannot be represented on a 5-km grid. Moreover, the simulated circulation lacks several drivers, close to the grounding line: the enhanced turbulence and buoyancy forcing produced by subglacial discharges of freshwater, and tidal forcing, which, with the K1 and M2 components would produce high amplitude tidal flow along the Kamb Ice Stream grounding line (MacAyeal, 1984). Therefore, circulation is stagnant close to the grounding line, except where, for example, at the WGZ, a strong flow of HSSW is driven close to the site.

To summarise, basal melt rates have been measured with high precision, semi-directly, using phase-sensitive radar, or radio-echo-sounding, (Marsh et al., 2016; Begeman et al., 2018; Whiteford et al., 2022; Price et al., 2025), although on small regions at a time, and shows a highly variable melting pattern. A synthesis of the measured basal melt rates is reported in Price et al. (2025) for the western part of the RIS cavity. The measurements, carried out in the western part, compares generally well with our pattern of simulated basal melting (Figure 4d), confirming two zones of melting, near the RIS front and near the grounding line, where a strong flow of HSSW, and seasonally of AASW, produces melting of up to $0.486 m/y$, compared with ~ 0.5 m/y simulated, and a low-melting central region,

where refreezing can occur. However, differences exist at the grounding line, such as at KIS1-2, where 0.145 m/y melting is not met by the model, as well as where subglacial channels are present, which are not included in the model ice morphology, and which produce extremely localised high melting.

Text S7. Intermodel comparison: MITgcm with ROMS output

The distribution of basal melting and attribution to different water masses show some differences: in ROMS, the whole RIS front is impacted by AASW, with strengthening in the Ross Island region, whereas in the MITgcm, only the latter region is affected. This produces a stronger seasonal cycle in ROMS (Figure S13g); AASW in ROMS is likely overrepresented due to ice shelf draft smoothing that is necessary with terrain-following z-coordinates, but frontal meltwater plumes may drive AASW under the RIS, by an isopycnal wedge mechanism (Malyarenko et al., 2019). Dinniman et al. (2018) simulate strong localized intrusions of mCDW (Figure S13), although in the ROMS simulations, mCDW intrudes at greater depth into the cavity; this strongly decreases the interaction with the ice shelf base. ROMS also simulates a stronger lateral salinity gradient between HSSW and LSSW near the mooring F site. The two models simulate a similar decadal variability of basal melting, highlighted as anomalies with respect to the climatology of monthly output (Figure S13). Dinniman et al. (2018) employs different lateral boundary conditions from a monthly climatological observation dataset (World Ocean Atlas 2001, WOA01) for θ, S, barotropic velocities from the Ocean Circulation and Climate Advanced Modelling project (OCCAM) and passive microwave satellite observations, (SSM/I), simulate a similar decadal oscillation in both salinity and basal melting. The reason, therefore, is more likely to be the atmospheric forcing, which in our model is ERA5 and in Dinniman et

al. (2018) is ERA-Interim, which may cause an excess of northward freshwater flux from sea ice, or an inaccurate precipitation vs evaporation balance on the continental shelf (Haumann et al., 2016).

Text S8. Sea ice budget calculations

Total sea ice growth in the MITgcm was calculated as the sum of four terms, that are contributions of energy fluxes, and internally converted to tendencies of sea-ice thickness changes: rate of change by ocean ice flux, rate of change by atmospheric – sea ice flux, rate of change by open-ocean – atmospheric fluxes, rate of change by flooding of the snow layer above sea ice. The tendencies of sea ice thickness rate of change were summed at monthly frequency over the surface area of each grid cell, over the regions where polynyas occur. The Terra Nova Bay (TNB) and RIS polynyas were defined by slicing rectangular regions from the ocean grid cells. Notice that sea ice production is calculated employing all but the snow flooding term since we are ultimately interested in the brine rejection occurring from the freezing of seawater. We calculated anomalies concerning a monthly climatology of sea ice production, excluding the months 'NDJF' since only melting occurs in that period. The time integral is calculated by a cumulative sum (running integral) of the monthly anomalies. Yearly average sea ice production during the period March-October is 610 km^3/y in the TNB and RIS polynyas (and the McMurdo polynya, for 1993-2018, and 850 km^3/y for all the continental shelf. The TNB production is 87 km^3/y, and the RIS production is 523 km^3/y. Sea ice production calculated by Tamura et al. (2016) for both polynyas is 380 $\pm$ 63, for 1992 - 2013. They employed a thin-ice threshold of 0.2 m to identify newly formed ice on remote-sensing data; for the same period, our simulated sea ice formation is 606 km^3/y. Notice that the threshold used in Tamura et al. (2016)

would not be applicable to our monthly-averaged output because of the fast thickening of newly formed ice. Drucker et al. (2011) employing microwave radiometers, estimated for the Ross Sea, summing TNB, RIS, and McMurdo Sound polynya, an average of 740 km^3/y, with an error of about 30%, which is compatible with our simulated value.

References

Adcroft, A., Hill, C., & Marshall, J. (1997). Representation of topography by shaved cells in a height coordinate ocean model. *Monthly Weather Review*, *125*(9), 2293–2315.

Arrigo, K. R., van Dijken, G. L., Ainley, D. G., Fahnestock, M. A., & Markus, T. (2002). Ecological impact of a large Antarctic iceberg. *Geophysical Research Letters*, *29*(7), 8–1.

Arzeno, I. B., Beardsley, R. C., Limeburner, R., Owens, B., Padman, L., Springer, S. R., ... Williams, M. J. (2014). Ocean variability contributing to basal melt rate near the ice front of Ross Ice Shelf, Antarctica. *Journal of Geophysical Research: Oceans*, *119*(7), 4214–4233.

Begeman, C. B., Tulaczyk, S. M., Marsh, O. J., Mikucki, J. A., Stanton, T. P., Hodson, T. O., ... King, M. A. (2018). Ocean stratification and low melt rates at the Ross Ice Shelf grounding zone. *Journal of Geophysical Research: Oceans*, *123*(10), 7438–7452.

Bergamasco, A., Defendi, V., Budillon, G., & Spezie, G. (2004). Downslope flow observations near Cape Adare shelf-break. *Antarctic Science*, *16*(2), 199–204.

Bergamasco, A., Defendi, V., Zambianchi, E., & Spezie, G. (2002). Evidence of dense water overflow on the Ross Sea shelf-break. *Antarctic Science*, *14*(3), 271–277.

Clough, J. W., & Hansen, B. L. (1979). The Ross ice shelf project. *Science*, *203*(4379), 433–434.

Dinniman, M. S., Klinck, J. M., Hofmann, E. E., & Smith, J., Walker O. (2018). Effects of Projected Changes in Wind, Atmospheric Temperature, and Freshwater Inflow on the Ross Sea. *Journal of Climate*, *31*(4), 1619-1635. Retrieved from `https://doi.org/10.1175/JCLI-D-17-0351.1` doi: 10.1175/JCLI-D-17-0351.1

Drucker, R., Martin, S., & Kwok, R. (2011). Sea ice production and export from coastal polynyas in the Weddell and Ross Sea. *Geophysical Research Letters*, *38*(17).

Fretwell, P., Pritchard, H. D., Vaughan, D. G., Bamber, J. L., Barrand, N. E., Bell, R., ... others (2013). Bedmap2: improved ice bed, surface and thickness datasets for Antarctica. *The Cryosphere*, *7*(1), 375–393.

Gordon, A. L., Orsi, A. H., Muench, R., Huber, B. A., Zambianchi, E., & Visbeck, M. (2009). Western Ross Sea continental slope gravity currents. *Deep Sea Research Part II: Topical Studies in Oceanography*, *56*(13-14), 796–817.

Haumann, F. A., Gruber, N., Münnich, M., Frenger, I., & Kern, S. (2016). Sea-ice transport driving southern ocean salinity and its recent trends. *Nature*, *537*(7618), 89–92.

Hellmer, H. H., & Olbers, D. J. (1989). A two-dimensional model for the thermohaline circulation under an ice shelf. *Antarctic Science*, *1*(4), 325–336.

Hersbach, H., Bell, B., Berrisford, P., Hirahara, S., Horányi, A., Muñoz-Sabater, J., ... others (2020). The ERA5 global reanalysis. *Quarterly Journal of the Royal Meteorological Society*, *146*(730), 1999–2049.

Holland, D. M., & Jenkins, A. (1999). Modeling thermodynamic ice–ocean interactions

at the base of an ice shelf. *Journal of Physical Oceanography*, *29*(8), 1787–1800.

Horgan, H. J., Stewart, C. L., Stevens, C., Dunbar, G., Balfoort, L., Schmidt, B. E., ... others (2025). A West Antarctic grounding-zone environment shaped by episodic water flow. *Nature geoscience*, 1–7.

Jacobs, S., Fairbanks, R. G., & Horibe, Y. (1985). Origin and evolution of water masses near the Antarctic continental margin: Evidence from H_2^{18} O / H_2^{16}O ratios in seawater. *Oceanology of the Antarctic continental shelf*, *43*, 59–85.

Jenkins, A. (2011). Convection-driven melting near the grounding lines of ice shelves and tidewater glaciers. *Journal of Physical Oceanography*, *41*(12), 2279–2294.

Jenkins, A., Hellmer, H. H., & Holland, D. M. (2001). The role of meltwater advection in the formulation of conservative boundary conditions at an ice–ocean interface. *Journal of physical oceanography*, *31*(1), 285–296.

Lawrence, J., Washam, P., Stevens, C., Hulbe, C., Horgan, H., Dunbar, G., ... others (2023). Crevasse refreezing and signatures of retreat observed at Kamb Ice Stream grounding zone. *Nature Geoscience*, *16*(3), 238–243.

Lellouche, J.-M., Greiner, E., Bourdallé-Badie, R., Garric, G., Melet, A., Drévillon, M., ... others (2021). The Copernicus global 1/12 oceanic and sea ice GLORYS12 reanalysis. *Frontiers in Earth Science*, *9*, 698876.

Lellouche, J.-M., Le Galloudec, O., Greiner, E., Garric, G., Regnier, C., Drevillon, M., & Le Traon, P. (2018). The Copernicus Marine Environment Monitoring Service global ocean 1/12 physical reanalysis GLORYS12V1: description and quality assessment. In *Egu general assembly conference abstracts* (Vol. 20, p. 19806).

Losch, M. (2008). Modeling ice shelf cavities in a z coordinate ocean general circulation

model. *Journal of Geophysical Research: Oceans*, *113*(C8).

Losch, M., Menemenlis, D., Campin, J.-M., Heimbach, P., & Hill, C. (2010). On the formulation of sea-ice models. Part 1: Effects of different solver implementations and parameterizations. *Ocean Modelling*, *33*(1-2), 129–144.

MacAyeal, D. R. (1984). Numerical simulations of the Ross Sea tides. *Journal of Geophysical Research: Oceans*, *89*(C1), 607–615.

Mack, S. L., Dinniman, M. S., Klinck, J. M., McGillicuddy Jr., D. J., & Padman, L. (2019). Modeling Ocean Eddies on Antarctica's Cold Water Continental Shelves and Their Effects on Ice Shelf Basal Melting. *Journal of Geophysical Research: Oceans*, *124*(7), 5067-5084. Retrieved from `https://agupubs.onlinelibrary.wiley.com/doi/abs/10.1029/2018JC014688` doi: 10.1029/2018JC014688

Malyarenko, A., Robinson, N., Williams, M., & Langhorne, P. (2019). A wedge mechanism for summer surface water inflow into the Ross Ice Shelf cavity. *Journal of Geophysical Research: Oceans*, *124*(2), 1196–1214.

Marsh, O. J., Fricker, H. A., Siegfried, M. R., Christianson, K., Nicholls, K. W., Corr, H. F., & Catania, G. (2016). High basal melting forming a channel at the grounding line of Ross Ice Shelf, Antarctica. *Geophysical Research Letters*, *43*(1), 250–255.

Marshall, J., Adcroft, A., Hill, C., Perelman, L., & Heisey, C. (1997). A finite-volume, incompressible Navier Stokes model for studies of the ocean on parallel computers. *Journal of Geophysical Research: Oceans*, *102*(C3), 5753–5766.

Marshall, J., Hill, C., Perelman, L., & Adcroft, A. (1997). Hydrostatic, quasi-hydrostatic, and nonhydrostatic ocean modeling. *Journal of Geophysical Research: Oceans*, *102*(C3), 5733–5752.

Padman, L., Howard, S. L., Orsi, A. H., & Muench, R. D. (2009). Tides of the northwestern Ross Sea and their impact on dense outflows of Antarctic Bottom Water. *Deep Sea Research Part II: Topical Studies in Oceanography*, *56*(13-14), 818–834.

Pochini, E. (2022). *Paleo and present oceanic modelling of the Ross Sea (Antarctica): evolution of water masses and ice shelf–ocean interactions during the last glacial cycle (21-0 ka)* (Doctoral dissertation). Retrieved from `https://hdl.handle.net/11368/3030770` (doi for the high resolution version: AAAAAAAA)

Price, D., Snodgrass, J., Rack, W., Purdie, H., Hulbe, C., Wild, C. T., ... others (2025). Basal reflectance and melt rates across the Ross Ice Shelf, Antarctica, from grounding line to ice shelf front. *Journal of glaciology*, *71*, e27.

Reerink, T. J., van de Berg, W. J., & van de Wal, R. S. W. (2016). OBLIMAP 2.0: a fast climate model–ice sheet model coupler including online embeddable mapping routines. *Geoscientific Model Development*, *9*(11), 4111–4132. Retrieved from `https://gmd.copernicus.org/articles/9/4111/2016/` doi: 10.5194/gmd-9-4111-2016

Shapiro, N. M., & Ritzwoller, M. H. (2004). Inferring surface heat flux distributions guided by a global seismic model: particular application to Antarctica. *Earth and Planetary Science Letters*, *223*(1-2), 213–224.

Stevens, C., Hulbe, C., Brewer, M., Stewart, C., Robinson, N., Ohneiser, C., & Jendersie, S. (2020). Ocean mixing and heat transport processes observed under the Ross Ice Shelf control its basal melting. *Proceedings of the National Academy of Sciences*, *117*(29), 16799–16804.

Stewart, C. L., Christoffersen, P., Nicholls, K. W., Williams, M. J., & Dowdeswell, J. A. (2019). Basal melting of Ross Ice Shelf from solar heat absorption in an ice-front

polynya. *Nature Geoscience*, *12*(6), 435–440.

Tamura, T., Ohshima, K. I., Fraser, A. D., & Williams, G. D. (2016). Sea ice production variability in Antarctic coastal polynyas. *Journal of Geophysical Research: Oceans*, *121*(5), 2967–2979.

Uotila, P., Goosse, H., Haines, K., Chevallier, M., Barthélemy, A., Bricaud, C., ... others (2019). An assessment of ten ocean reanalyses in the polar regions. *Climate Dynamics*, *52*(3-4), 1613–1650.

Whiteford, A., Horgan, H., Leong, W., & Forbes, M. (2022). Melting and refreezing in an ice shelf basal channel at the grounding line of the Kamb Ice Stream, West Antarctica. *Journal of Geophysical Research: Earth Surface*, *127*(11), e2021JF006532.

Zotikov, I. A. (1979). *Antifreeze-Thermodrilling for Core through the Central Part of the Ross Ice Shelf (J-9 Camp), Antarctica* (Tech. Rep.). Cold Rregions Research And Engineering Lab Hanover NH.

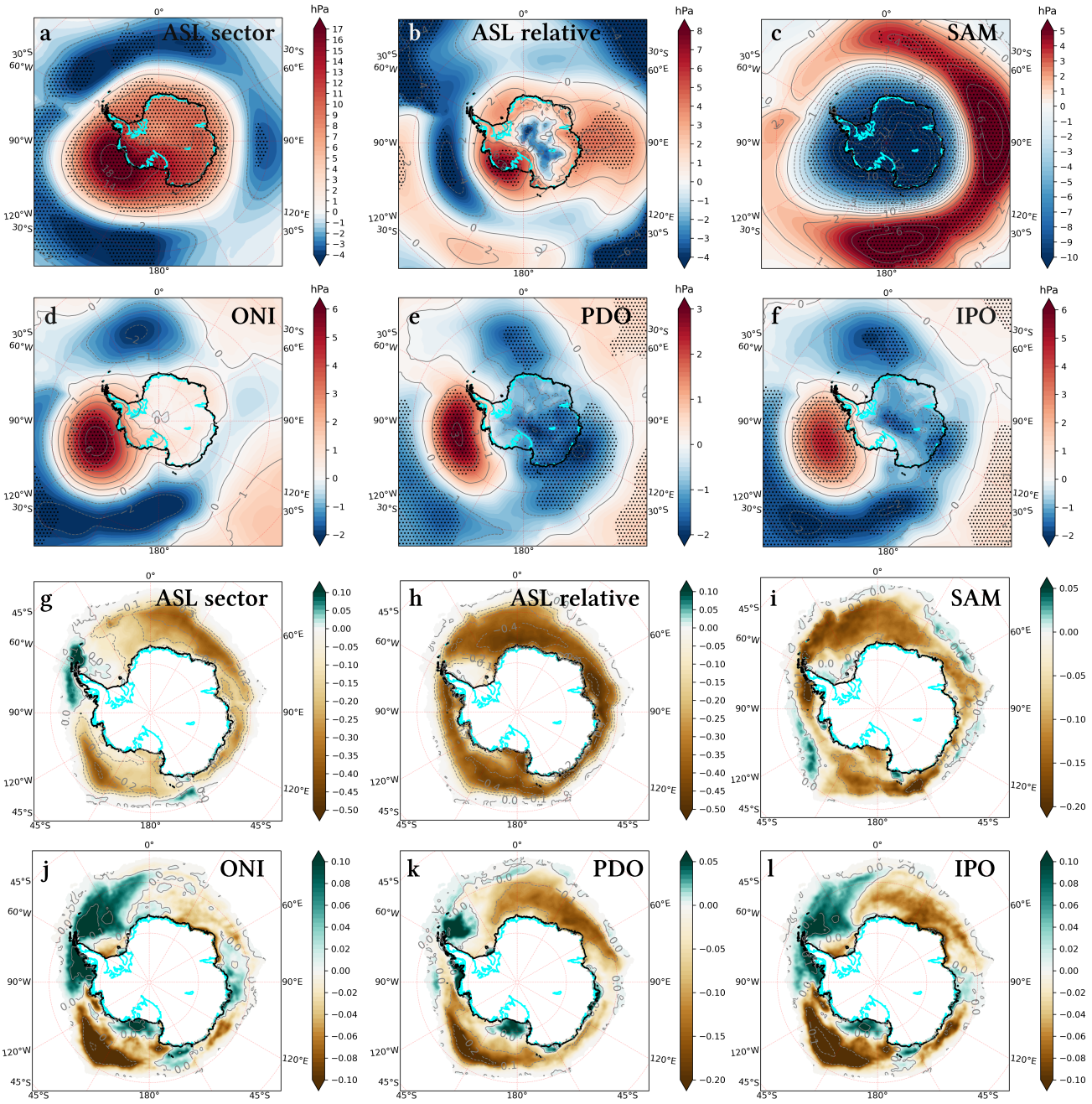


Figure S1. Linear regression of the monthly mean sea-level pressure (a-f) and the monthly-mean sea ice concentration (g-l) on the following indices: (a,g) Amundsen Sea Low sector average, (b,h) Amundsen Sea Low pressure relative to the centre minimum; (c,i) Southern Annular Mode; (d,j) Ocean Niño Index; (e,k) Pacific Decadal Oscillation; (f,l) Interdecadal Pacific Oscillation. Positive regressed pressure yields anticyclonic surface-wind anomalies. Pressure and sea ice concentration are monthly fields from ERA5 (1990-2019, Hersbach et al., 2020). The cyan line represents the grounding line.

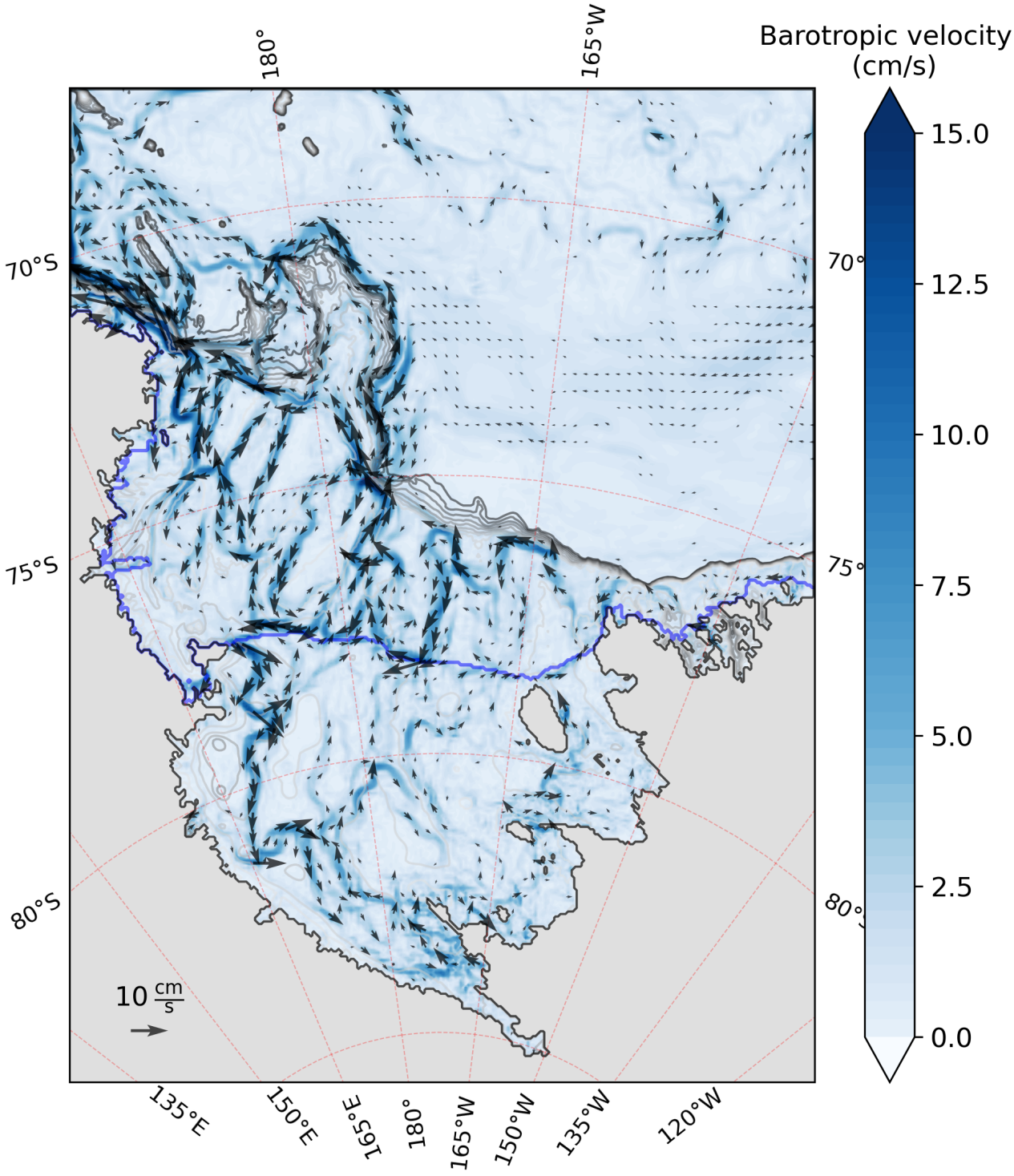


Figure S2. Barotropic velocity (cm/s) time-averaged over the simulation period (1993-2018). The coastline is indicated in dark grey, while the blue line shows the ice shelves' margins.

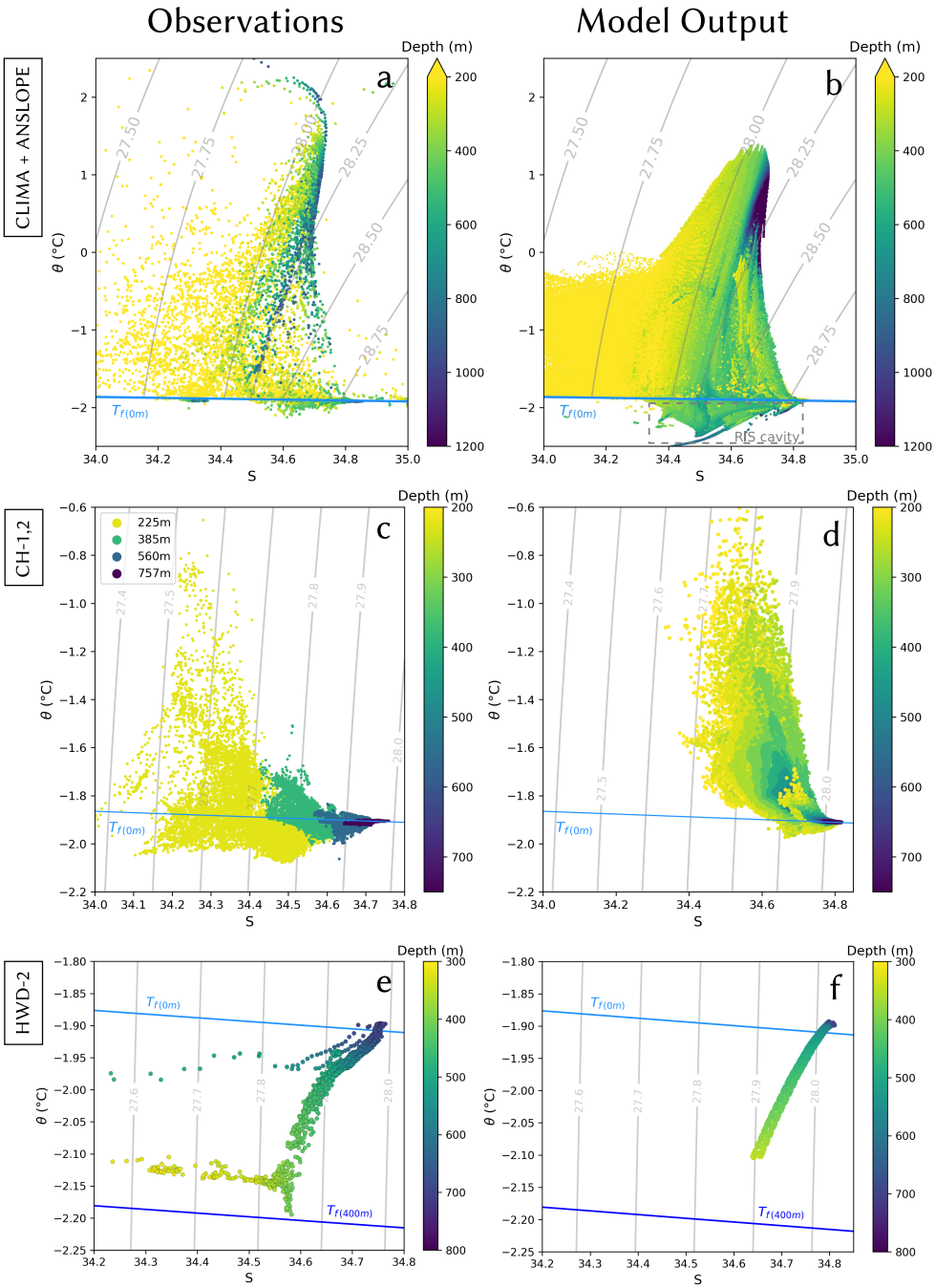


Figure S3. Data-model hydrographic (θS) comparison. (a) CTD measurements from CLIMA (1997-2006) and AnSlopeIII (2004) projects over the Ross Sea continental shelf and slope shallower than 1200 m. (b) Simulated monthly fields over the continental shelf, slope (shallower than 1200 m) and RIS cavity, over the summer months ("DJF") of 1993-2018. (c) Mooring data from year-round borehole measurements at location CH1,2 (see Figure 1a), over 2011-2014 (Stewart et al., 2019). (d) Simulated daily fields from the same location and period. (e) CTD measurements from borehole site HWD-2 (see Figure 1a) over December 2017 (Stevens et al., 2020). (f) Simulated daily fields from the same location and period, interpolated at 10 m intervals.

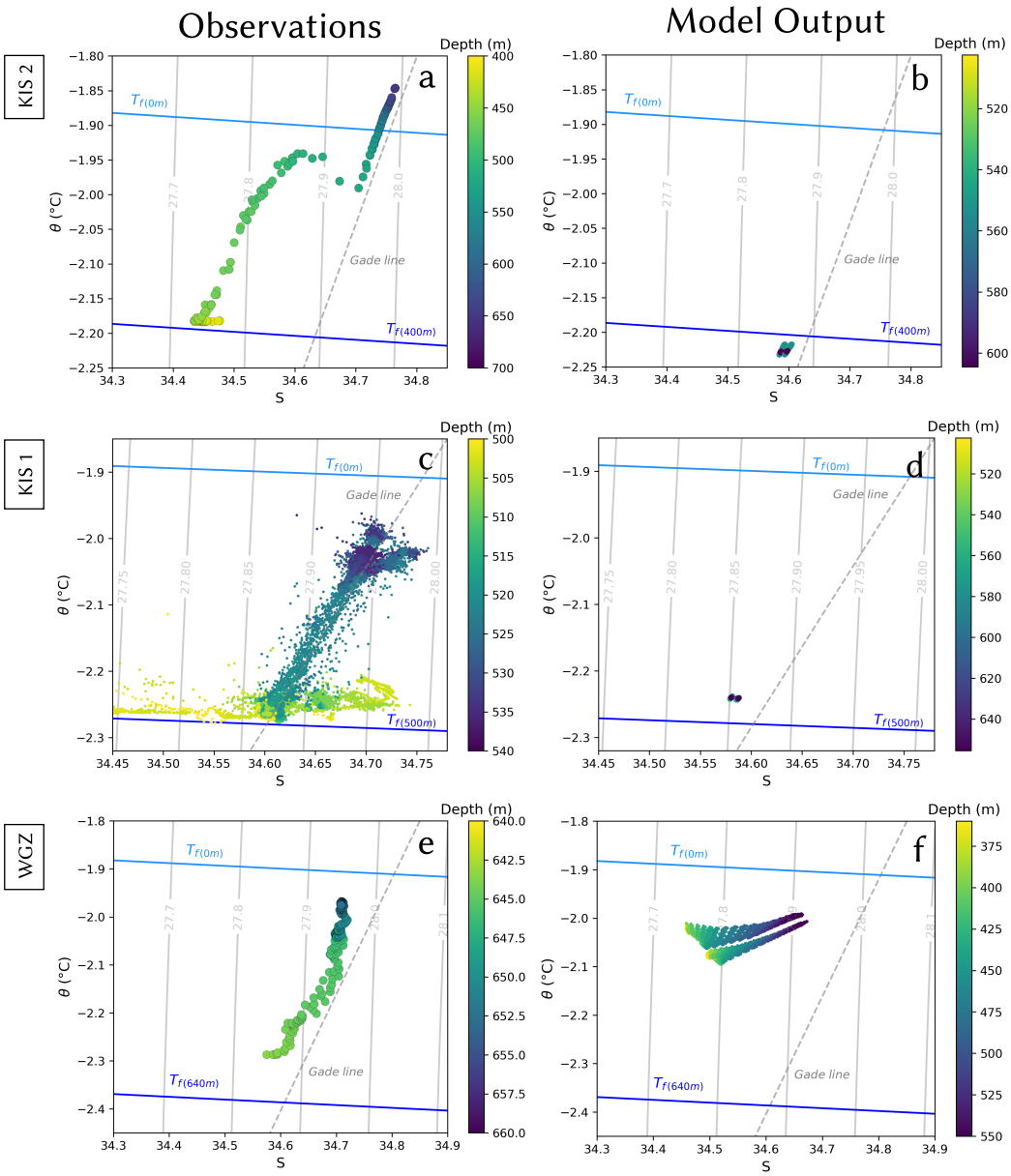


Figure S4. Data-model hydrographic comparison at borehole sites near the grounding line. CTD data from borehole (a) KIS 2 (Horgan et al., 2025), summer 2021-2022; (c) KIS 1 (Lawrence et al., 2023), summer 2019; (e) WGZ (Begeman et al., 2018), summer 2015 (see locations in Figure 1). (b),(d), (f) Simulated daily fields at the same locations as (a),(c),(e), over the summer months ("DJF") of: 2015 for (f), and for the last year of simulation (2018), for (a) and (c). Notice the different depth range and the lack of variability in simulated θS in (b), (d).

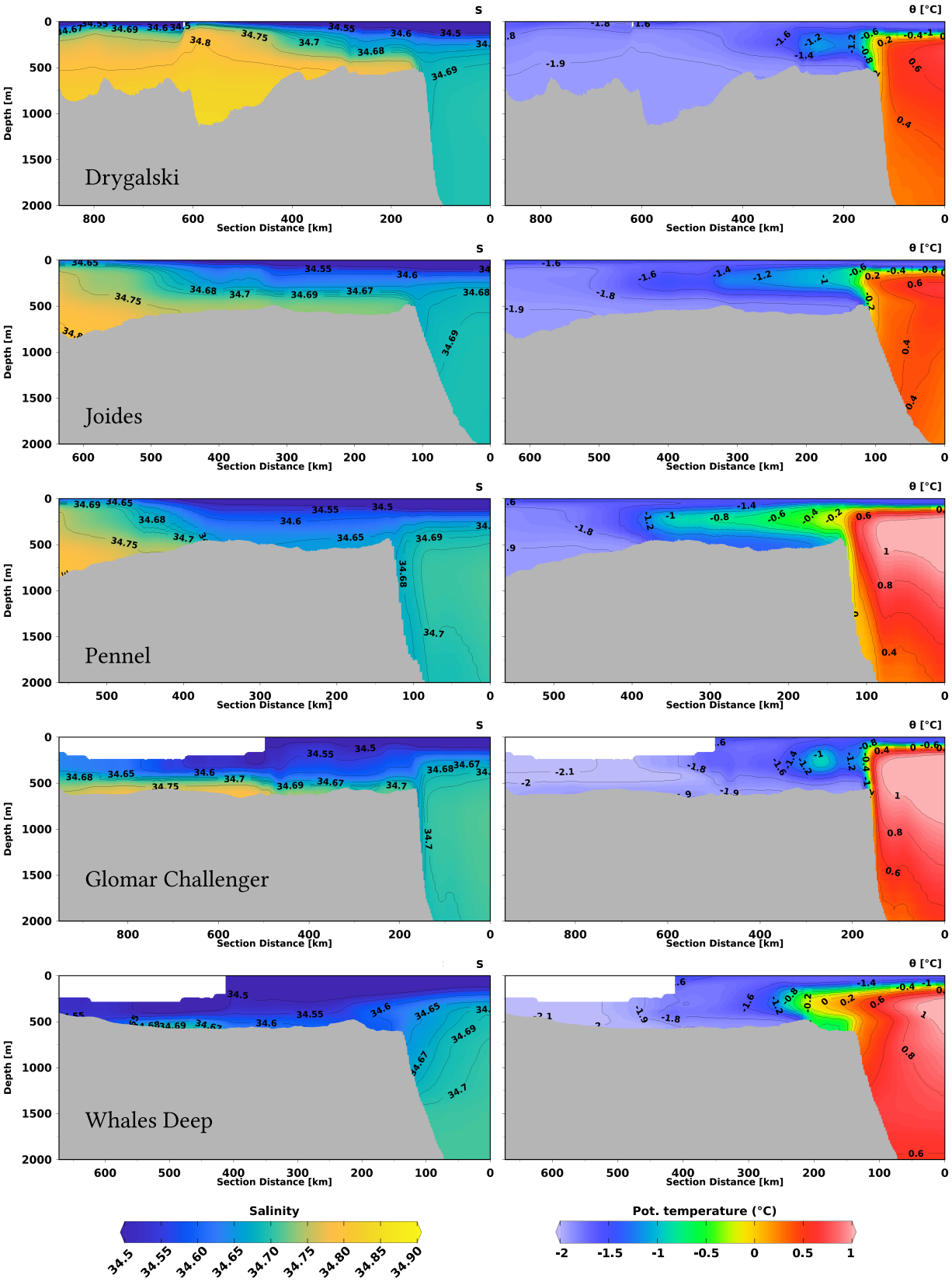


Figure S5. Vertical sections of time-averaged simulated salinity (left column) and potential temperature (right column) along the main troughs of the Ross Sea. Averages are over the simulation period (1993-2018). Grey region is the continental shelf; the white patch is the RIS.

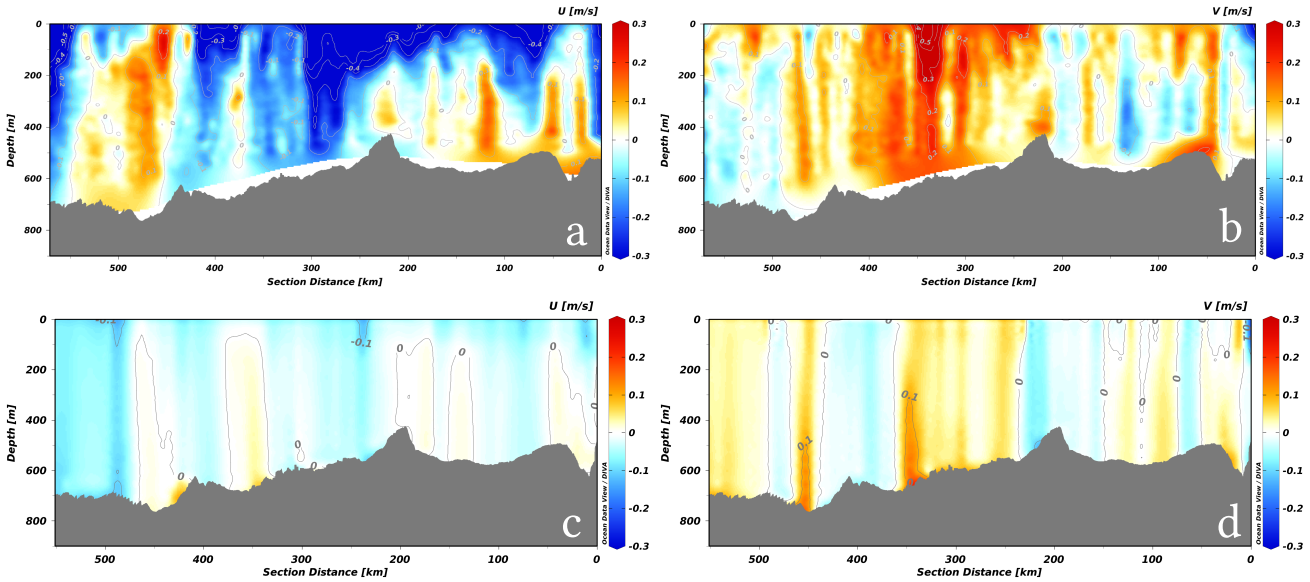


Figure S6. Model-observation comparison along the RIS front. (a,b) Velocity measurements (vessel mounted acoustic doppler current profiler vmADCP, 2017 PNRA expedition), zonal (a) and meridional (b) components. (c,d) The same quantities as simulated in the present work.

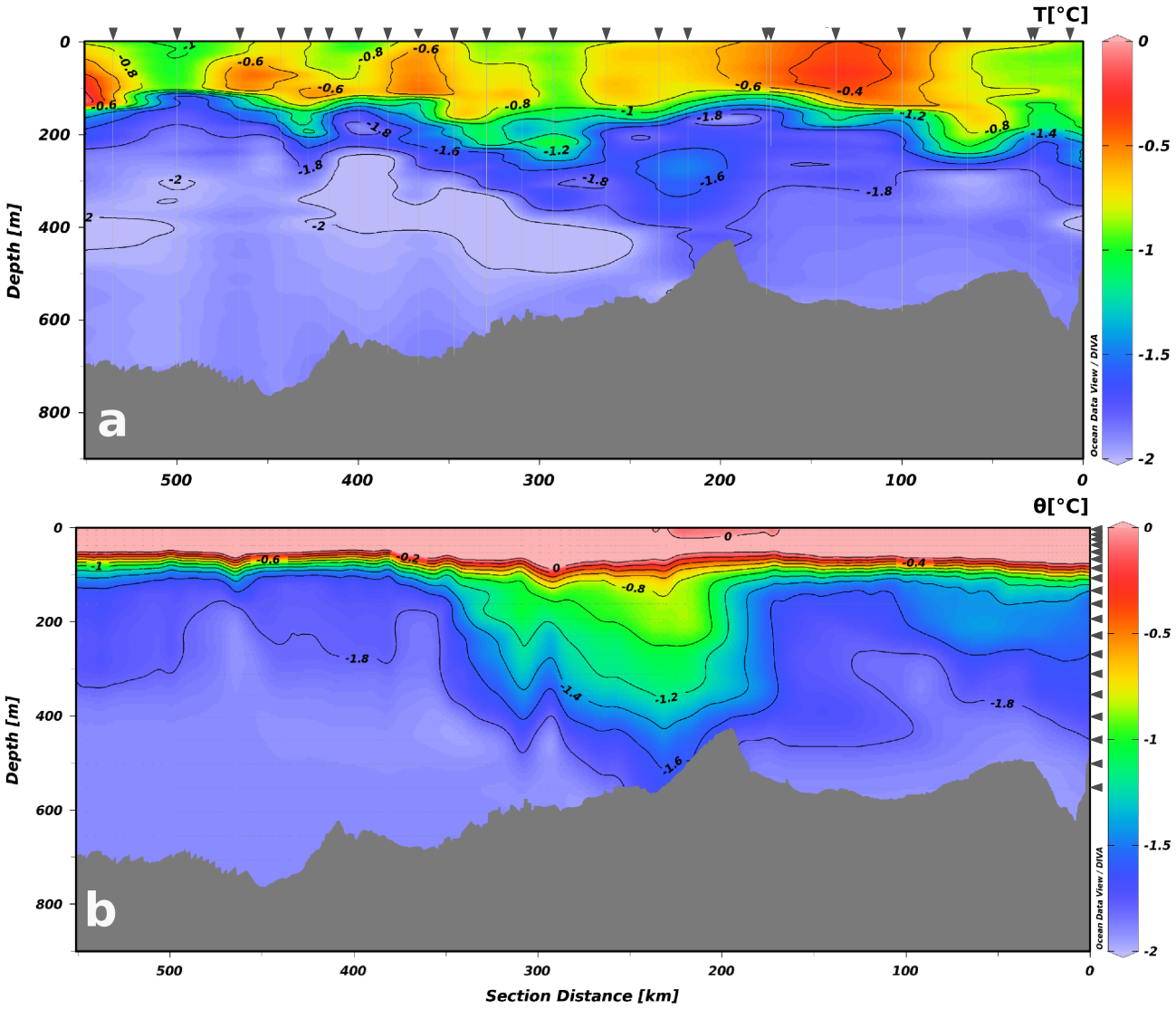


Figure S7. Austral summer temperature sections summer: (a) XBTs measurements, (b) simulated in this study. Note the sampling points visible as thin grey dotted lines: casts have high vertical resolution and coarse horizontal resolution; the opposite for simulated output.

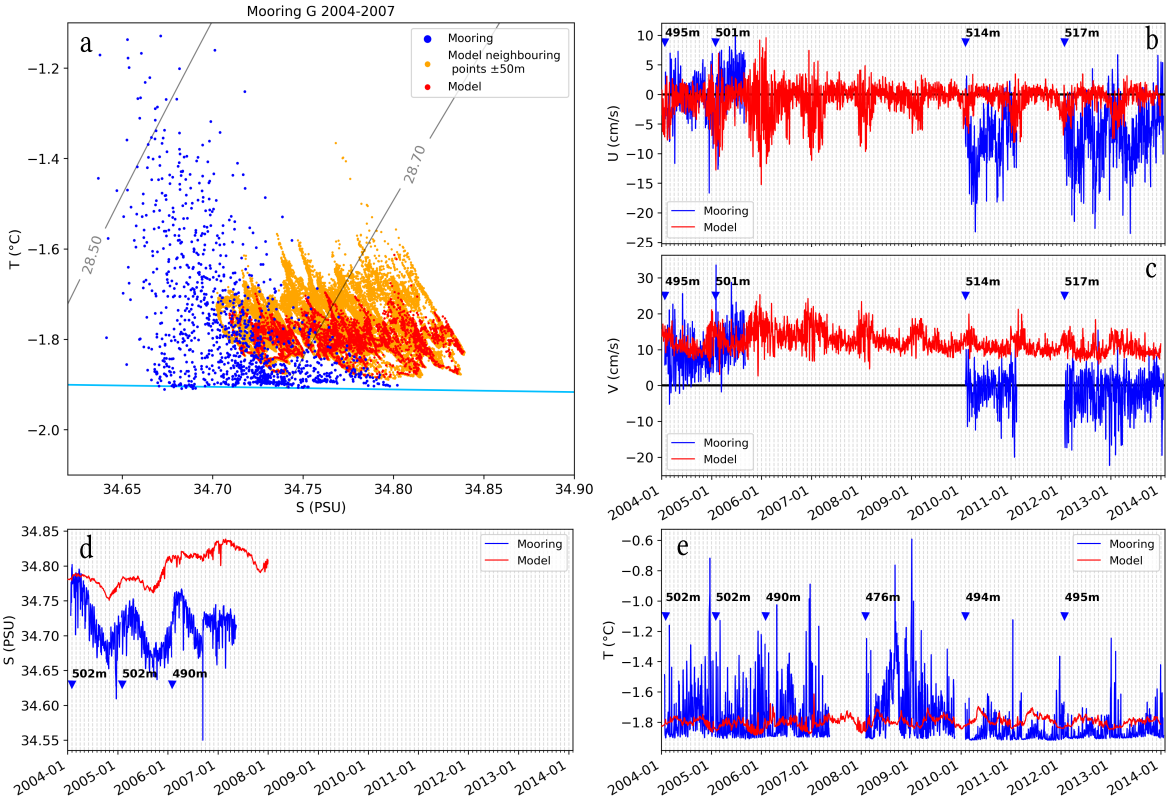


Figure S8. Model-observation comparison at mooring G in the Drygalski Trough. Model (red: pointwise, orange: neighbouring points) vs observations (blue, in-situ temperature from Seabird instrument) at daily frequency. (a) TS plot, (b) zonal and (c) meridional velocity, (d) salinity (e) temperature.

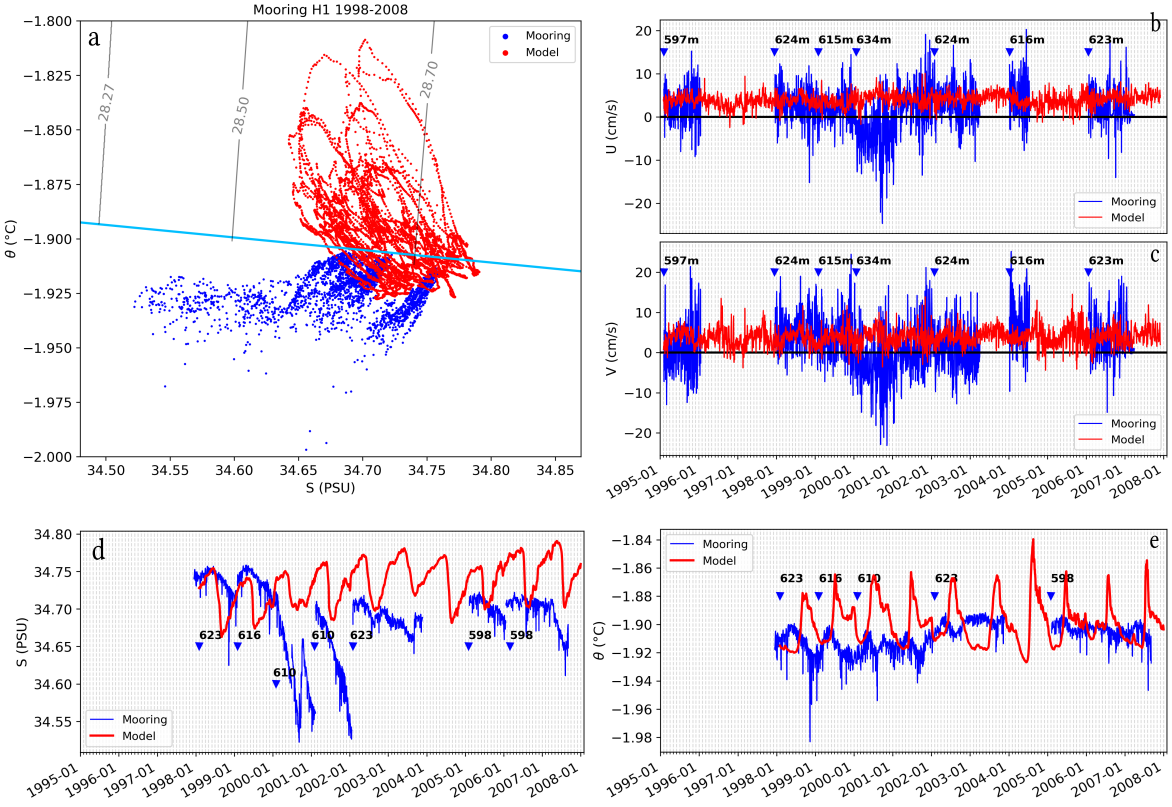


Figure S9. Model-observation comparison at mooring H1 site in the Glomar Challenger Trough. Model (red, orange) vs observations (blue) at daily frequency. (a) θ, S plot, (b) zonal and (c) meridional velocity, (d) salinity, (e) potential temperature.

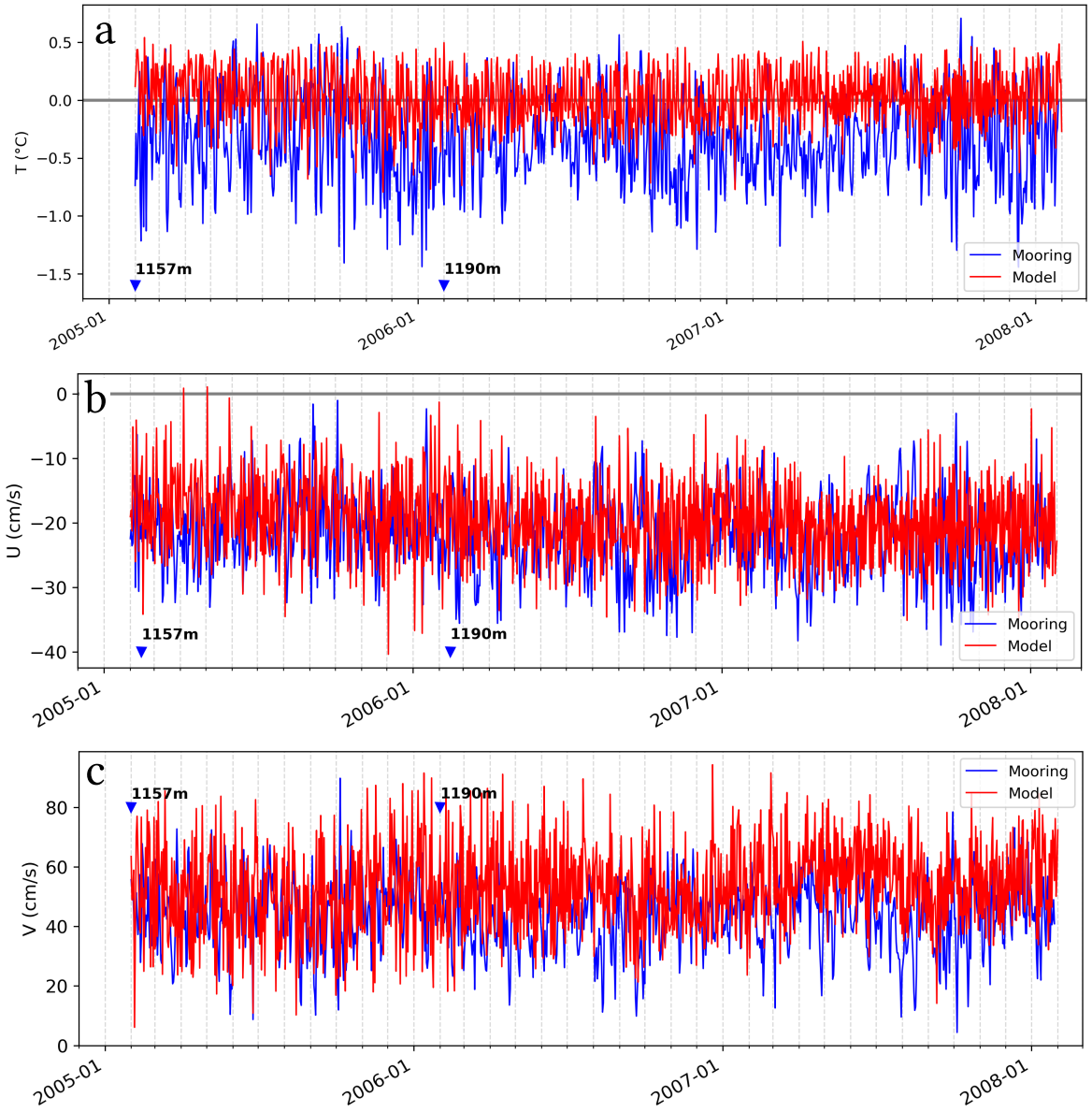


Figure S10. Model-observation comparison at mooring H3, on the continental slope (location Figure 1a). Model (red, orange) vs observations (blue) at daily frequency. (a) In-situ temperature, (b,c) zonal and meridional velocities. Velocities averaged over 3x3 grid points are masked over water depth equal or shallower than the instrument depth (∼1200m), to capture the shallower portion of the slope.

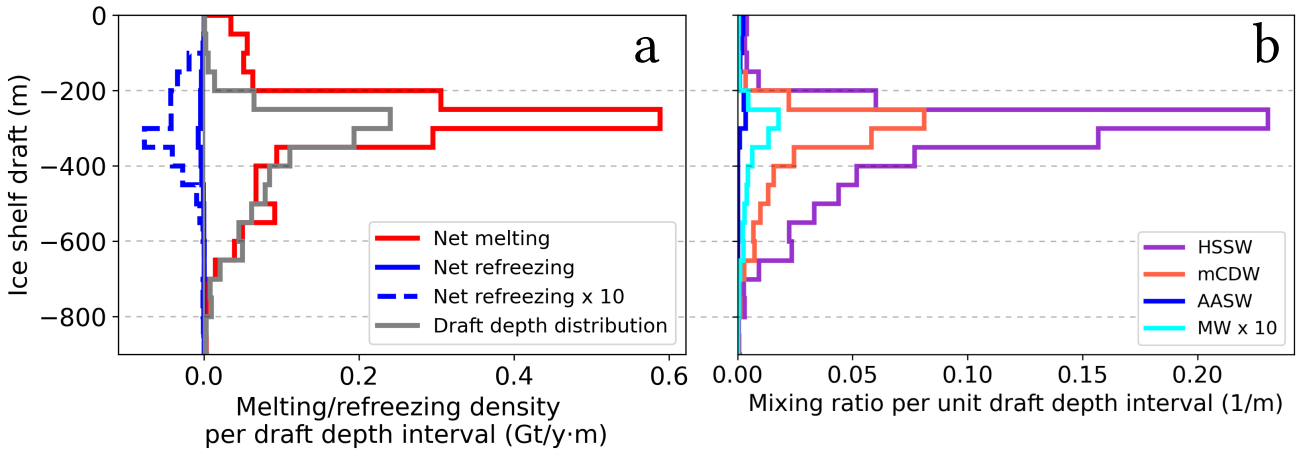


Figure S11. (a) Distribution of the simulated RIS basal melting and refreezing per metre of draft depth (Gt/y m), overlaid to the distribution of RIS draft in depth (grey). (b) Distribution in depth of the water masses mixing ratios at RIS draft level, per unit of draft depth (1/m).

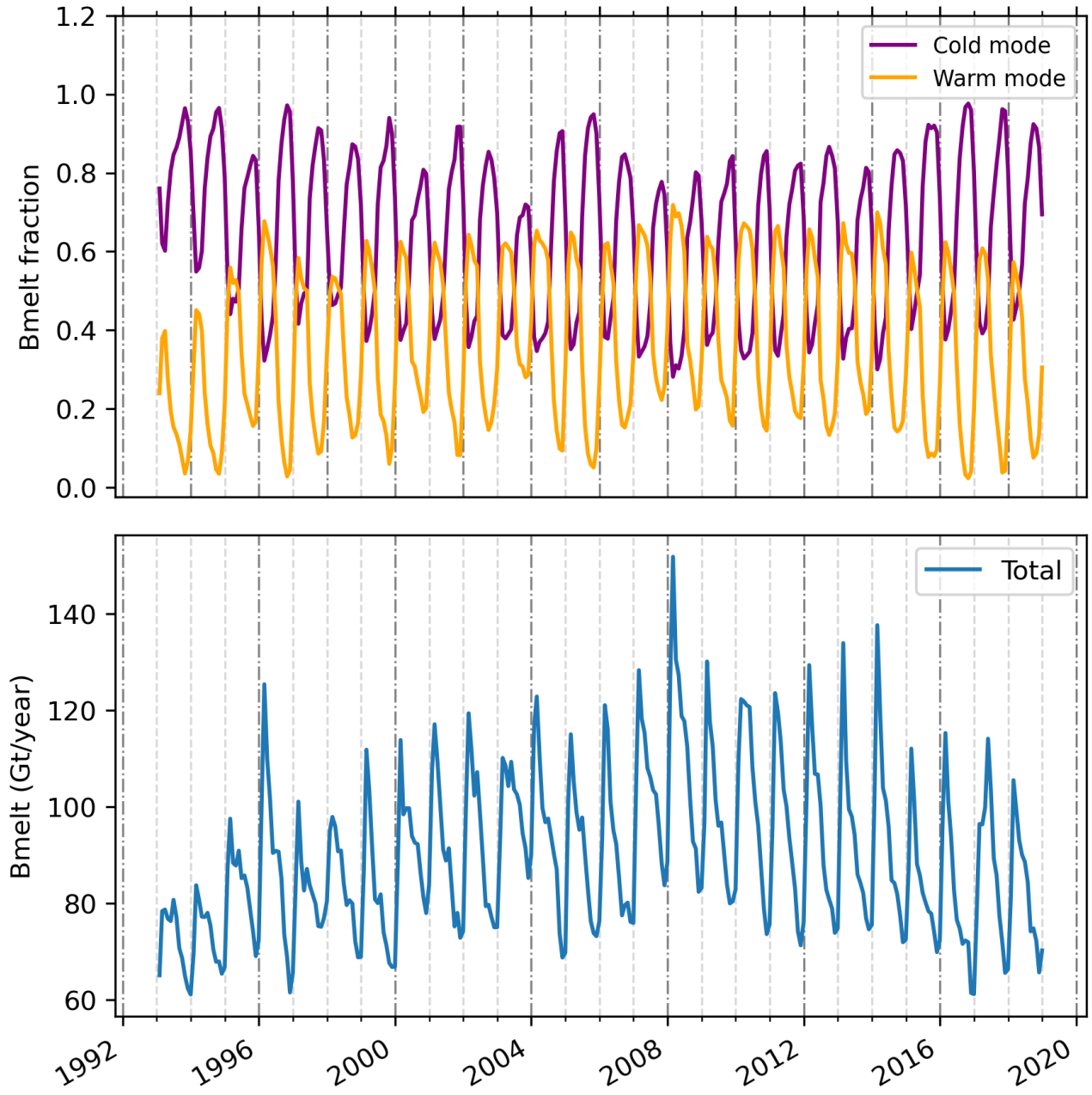


Figure S12. Upper panel: simulated integrated basal melting partitioned according to the surface freezing point ("supercooling criterion", Mack et al., 2019): "cold" mode represents all water masses colder than the surface freezing point, calculated with the in-situ salinity, "warm" mode represents those above it. Lower panel: simulated integrated basal melting.

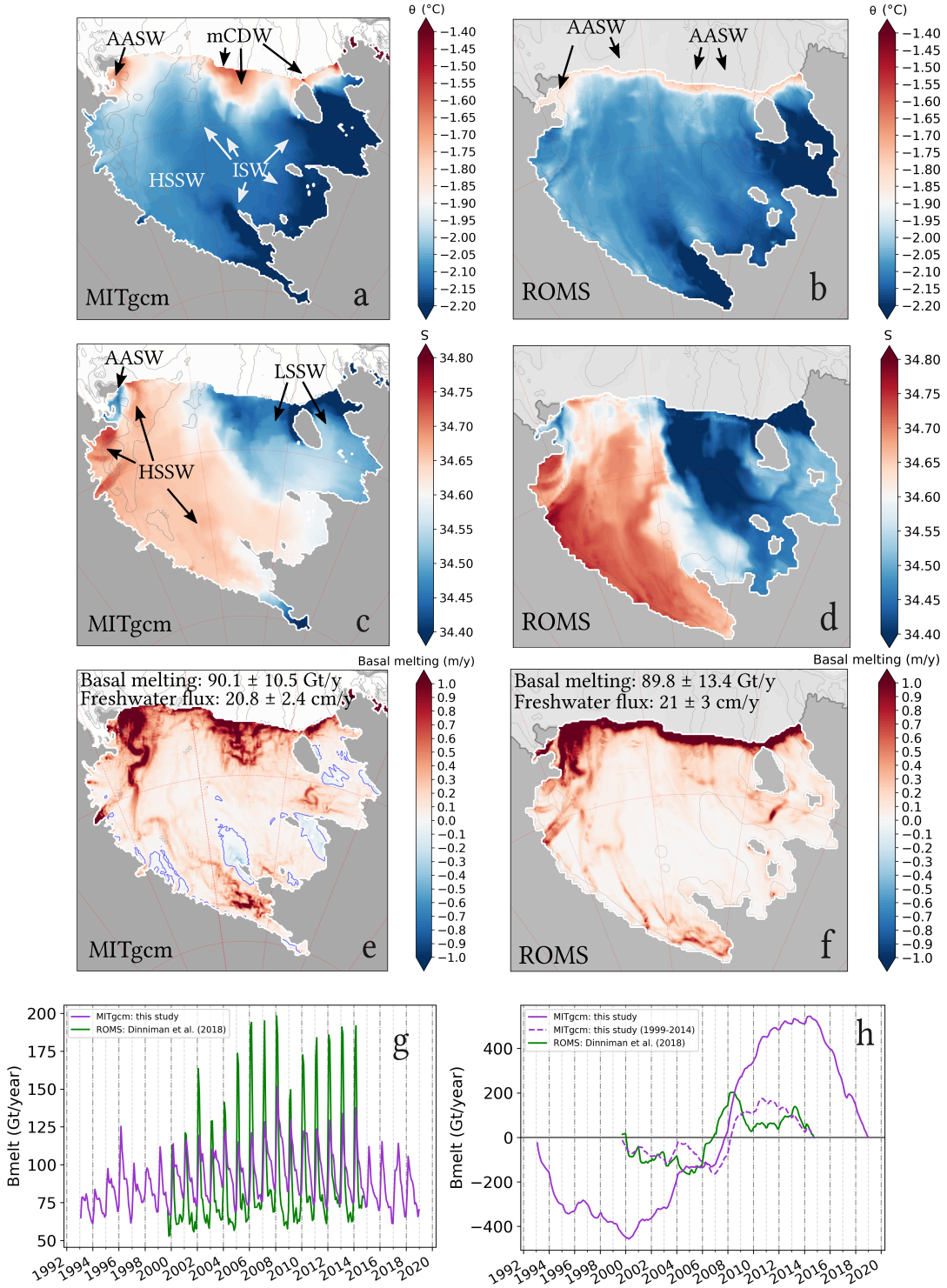


Figure S13. Comparison of the mean water properties at the RIS draft from the MITgcm simulations (this study 1993-2018) and ROMS simulations (ROMS simulations 1999-2014, Dinniman et al., 2018). Both are run with transient forcing from ERA5 reanalysis, interactive sea ice and thermodynamically interactive ice shelf. Time-averaged values at ice shelf draft: (a,b) potential temperature; (c,d) salinity; (e,f) basal melting rate. (g) Comparison of the integrated basal melting of the RIS. (h) Cumulative sum of the monthly basal melting anomaly with respect to a monthly climatology based on the same respective simulated basal melting.

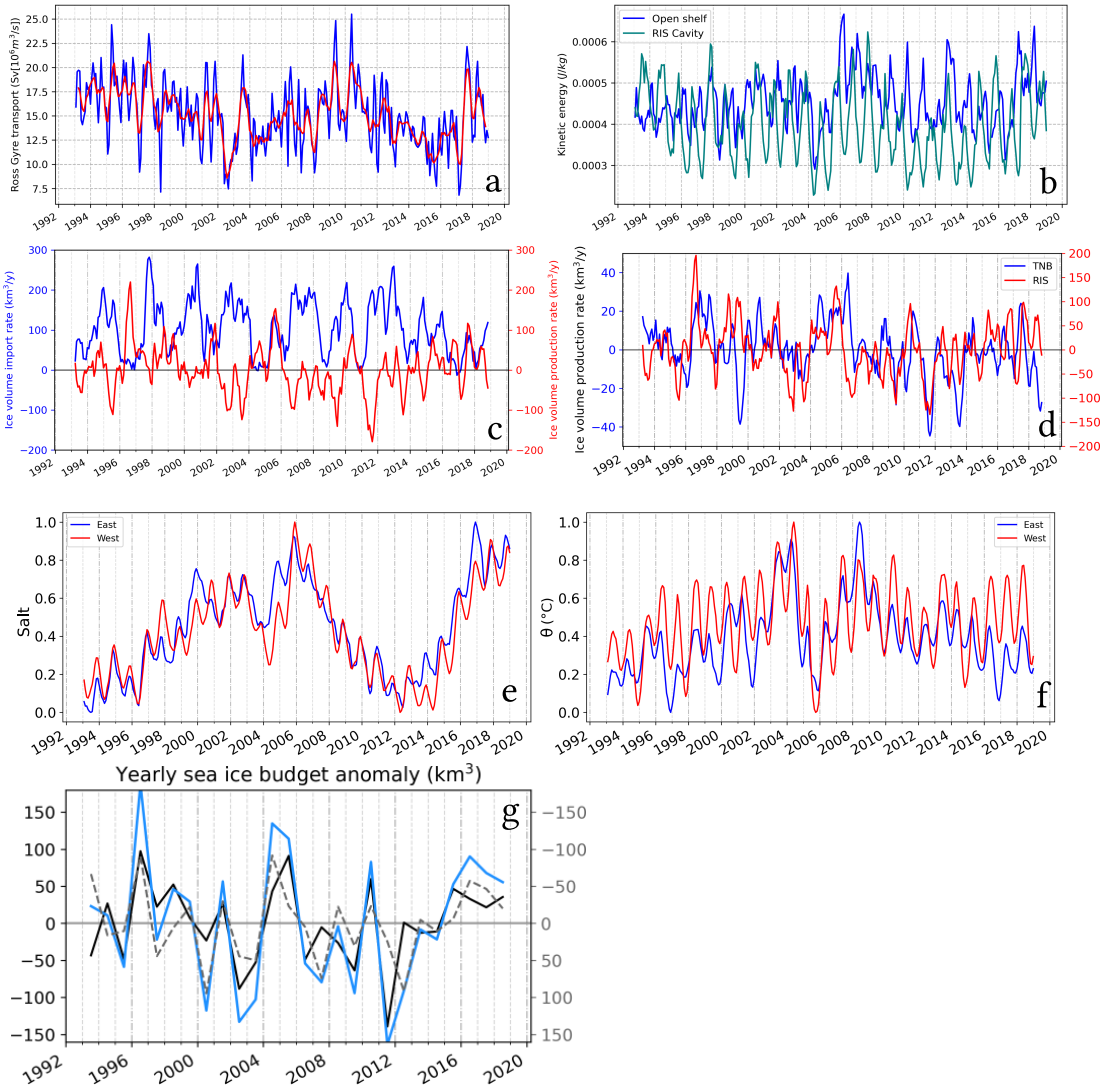


Figure S14. (a) Ross Sea gyre transport (Sv); blue line is monthly transport, red line is the 5-month moving average. (b) Barotropic circulation strength (specific kinetic energy) averaged over the open continental shelf (blue) and in the Ross ice shelf cavity (green). (c) Rate of annual import of sea ice along a 100 km section in the Eastern Ross sea continental shelf (blue) vs sea ice production/melting anomaly in the Terra Nova Bay and the Ross ice shelf polynya. (d) Sea ice monthly production rate anomaly in Terra Nova Bay (blue) and Ross ice shelf polynya (red). Notice the change in scale, as the Ross ice shelf polynya sea ice production is higher than Terra Nova Bay due to the larger area. (e),(f) normalised S and θ averaged over the Western (red) and Eastern (blue) continental shelf. (g) Annual-mean sea-ice production anomaly (km^3/y) in polynyas (solid black), annual-mean imported sea ice into the eastern Ross Sea continental shelf (grey dash, reversed y-axis), and the net anomaly (light blue).

Table S1. Endpoints employed in the mixing method

Water mass	θ (°C)	S (psu)
HSSW	-1.9	34.8
mCDW	-1	34.5
AASW	-0.5	34.3
MW	-95.2 [a]	0

[a] "Virtual" temperature (see section 2.2.1).

Table S2. Reported basal melting (integrated) and basal freshwater (averaged) over the RIS draft. The first section reports estimates based on numerical ocean models found in the literature. The second section reports estimates based on indirect satellite observation. Listings are ordered from the oldest to the most recent. Basal melting and freshwater flux values are as reported in the references.

Study	Basal melting (Gt/y)	Freshwater Flux (cm/y)
Dinniman et al., (2011)	72.9	15.3
Timmerman et al., (2012)	260	N.a.
Kusahara and Hasumi (2013)	110.7	N.a.
Dinniman et al., (2015)	66.7	14
Arzeno et al., (2018)	38	32
Dinniman et al., (2018)	89.8±13.4	21 ± 3
Naughten et al., (2018) MetROMS	53.8	12
Naughten et al., (2018) FESOM HR	112	24
Mack et al., (2019)	102	21.4
Richter et al., (2020)	69.1	15
This study	**90 ± 10**	**21.8 ± 2.4**
Depoorter et al., (2013)	34	8±6
Rignot et al., (2013)	48 ± 24	10 ± 7
Moholdt et al., (2014)	50	N.a.
Liu et al., (2015)	27 ± 22	10 ± 0
Adusumilli et al., (2020)	80 ± 82	26 ± 27
Jourdain et al., (2020) (local/non-local calibration)	49/54	11.3/12.6

Table S3. Main model parameters

GENERAL PARAMS	
Reference Density (Boussinesq)	1028. kg/m^3
Specific heat capacity water	3.994 kJ/kg $\cdot$ K
Drag coefficient (bottom/ice shelf): Cd	1.5 E-3
Lateral boundaries	Free-slip
Bottom boundary	No-slip
Vertical tracer diffusivity T,S	5.0 E-6
Harmonic Leith viscosity	1.0
Biharmonic Leith viscosity	0.1
Vertical eddy viscosity	1.0 E-4
Equation of State	MDJWF
Advection Scheme	33
Base Timestep	600 s
SHELFICE_PARAMS (ice shelves)	
SHELFICEuseGammaFrict	True
no_slip_shelfice	False
SHELFICEwriteState	True
SHELFICEboundaryLayer	True
SHELFICEconserve	True
SHELFICEadvDiffHeatFlux	True
SHELFICEselectDragQuadr	2
SHELFICEthetaSurface	-20 °C
rhoShelfice	917 kg/m^3
SHELFICEheatCapacity_Cp	2.0 kJ/kg $\cdot$ K
SHELFICElatentHeat	$3.34 \cdot 10^5$ J/kg $\cdot$ K
OBCS_PARAMS (open bounaries)	
Sponge Thickness	8
Relaxation time (inner)	31536000 s
Relaxation time (outer)	604800 s
Seaice sponge thicknes	4
Seaice relaxation time (inner)	31536000 s
Seaice relaxation time (outer)	604800 s